# Simulated Kelvin–Helmholtz Waves over Terrain and Their Microphysical Implications

ROBERT CONRICK AND CLIFFORD F. MASS

*Department of Atmospheric Sciences, University of Washington, Seattle, Washington*

QI ZHONG

*China Meteorological Administration Training Center, Beijing, China*

(Manuscript received 1 March 2018, in final form 30 May 2018)

ABSTRACT

Two Kelvin–Helmholtz (KH) wave events over western Washington State were simulated and evaluated using observations from the Olympic Mountains Experiment (OLYMPEX) field campaign. The events, 12 and 17 December 2015, were simulated realistically by the WRF-ARW Model, duplicating the mesoscale environment, location, and structure of embedded KH waves, which had observed wavelengths of approximately 5 km. In simulations of both cases, waves developed from instability within an intense shear layer, caused by low-level easterly flow surmounted by westerly winds aloft. The low-level easterlies resulted from blocking by the Olympic Mountains in the 12 December case, while in the 17 December event, the easterly flow was produced by the synoptic environment. Simulated microphysics were evaluated for both cases using OLYMPEX observations. When the KH waves were within the melting level, simulated microphysical fields, such as hydrometeor mixing ratios, evinced considerable oscillatory behavior. In contrast, when waves were located below the melting level, the microphysical response was attenuated. Turning off the model's microphysics scheme and latent heating resulted in weakened KH wave activity, while removing the Olympic Mountains eliminated KH waves in the 12 December event but not the 17 December case. Finally, the impact of several microphysics parameterizations on KH activity was evaluated for both events.

## 1. Introduction

Kelvin–Helmholtz (KH) waves have been observed in a variety of atmospheric settings, including cumulonimbus anvils (Petre and Verlinde 2004), sea breeze circulations (Sha et al. 1991), and within midlatitude baroclinic systems and fronts (e.g., Wakimoto et al. 1992; Houze and Medina 2005; Friedrich et al. 2008; Houser and Bluestein 2011; Medina and Houze 2015, 2016; Barnes et al. 2018). KH waves have also been reported in regions of complex terrain, where terrain-enhanced vertical wind shear can initiate KH instability (e.g., Geerts and Miao 2010; Medina and Houze 2016). Terrain-induced shear can originate from a number of mechanisms, including the lifting of a low-level shear layer (Houze and Medina 2005), deceleration of low-level flow by terrain (Medina and Houze 2016), and downslope flows (Geerts and Miao 2010).

An important question regards the influence of KH waves on moist physics, and particularly whether simulating the impacts of such waves is required for realistic modeling of orographic precipitation. Based on observations from two field campaigns in regions of complex terrain, Houze and Medina (2005) suggested that upward motion in KH waves leads to enhanced depositional growth, which can increase orographic precipitation. Houser and Bluestein (2011), examining dual-polarimetric radar over Oklahoma, found that the upward motion of KH waves has a significant impact on microphysical processes, with riming enhanced because of either an increase in turbulent motions or from the introduction of supercooled water into a region of frozen particles. Neither of these studies quantified the impacts of KH waves on precipitation at the surface.

Barnes et al. (2018) described the influence of KH waves on radar-observed fields and precipitation during the Olympic Mountains Experiment (OLYMPEX) field

*Corresponding author*: Robert Conrick, rconrick@uw.edu

DOI: 10.1175/JAS-D-18-0073.1

campaign (Houze et al. 2017). They showed KH-related modulation of rain rate when the waves were below the melting level, along with impacts on mass-weighted mean drop diameter, reflectivity, and fall speed. Additionally, they described KH waves occurring within and above the melting layer but did not explore the microphysical implications in these cases.

A number of papers have applied numerical modeling to the study of KH instability (e.g., Fritts 1979; Sykes and Lewellen 1982; Droegemeier and Wilhelmson 1987; Fritts et al. 1996; Smyth 2004; Zhou and Chow 2013; Nakanishi et al. 2014), with most using idealized or dry models. Large-eddy simulation (LES) experiments have investigated KH instability in a variety of real-world cases, including in a mesoscale convective system (MCS) over southern England (Browning et al. 2012), within a hurricane boundary layer (Nakanishi and Niino 2012; Na et al. 2014), during frontogenesis (Samelson and Skyllingstad 2016), and for stratified flow over terrain (Sauer et al. 2016). Recent studies have used full-physics NWP models to simulate KH waves. Mahalov et al. (2011), using the Weather Research and Forecasting (WRF) Model, demonstrated that terrain-induced KH waves in the upper troposphere were not resolved at 3-km horizontal grid spacing but were at 1 km. Efimov (2017) used the WRF Model to simulate KH waves over Crimea, and Trier et al. (2012) simulated turbulence arising from KH instability in a winter cyclone. Thompson (2007) simulated the formation of KH instability in a sea-breeze front using the U.S. Navy's Coupled Ocean–Atmosphere Mesoscale Prediction System (COAMPS) model. Finally, Kudo (2013) demonstrated that KH waves can be generated when cooling from sublimating snow reduces atmospheric stability.

Few studies have simulated KH waves and their microphysical impacts over complex terrain, and this study attempts to do so. Specifically, the WRF Model is used to simulate two cases of KH waves over the Olympic Mountains of Washington State during OLYMPEX, with the goal of answering several questions:

1) How do changing synoptic conditions initiate and control the evolution of KH waves?
2) How are KH waves modified by different mesoscale environments (e.g., over the ocean, windward slopes, crests)? Are there key mesoscale controls on KH wave formation?
3) What resolution is required to realistically simulate KH waves in WRF? Are KH waves sensitive to the selection of microphysics schemes?
4) What are the microphysical impacts of KH waves during orographic precipitation events? How do simulated modulations in precipitation and microphysical quantities in simulated KH waves compare to those observed during the OLYMPEX project?

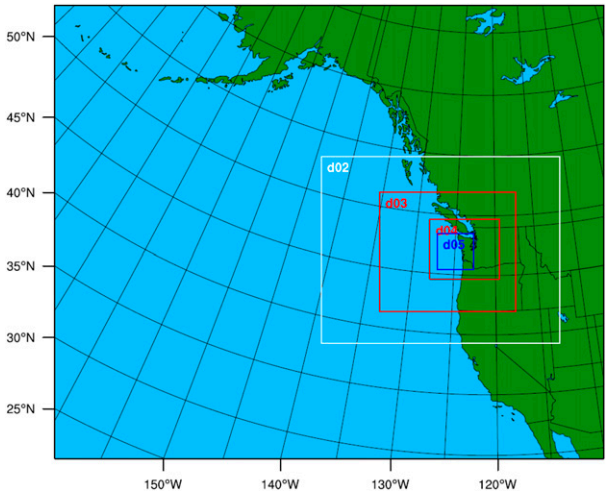


FIG. 1. Map of the WRF-ARW domains used in this study. The outer domain has 36-km grid spacing, with d02, d03, d04, and d05 domains using 12-, 4-, and 1.33-km and 444-m grid spacing, respectively.

Section 2 provides an overview of model configuration and data used. Sections 3 and 4 present results and analysis of the simulations, and section 5 describes the results of parameterization experiments. Section 6 offers concluding remarks.

## 2. Model configuration and observations

This study uses the Advanced Research version of WRF (WRF-ARW; Skamarock et al. 2005, 2008), version 3.8.1. A 36–12–4–1.33–0.444 km domain configuration is applied with 51 vertical levels,[1] with the innermost domains centered over the Olympic Peninsula of Washington State (Fig. 1). Initial and 3-h boundary conditions are from the NOAA/National Weather Service Global Forecast System (GFS) 0.25° gridded analysis. Since new GFS data are available every 6 h, only forecast hours 0000 and 0300 are used for boundary conditions and nudging.

Grid nudging on the 36-km domain ensures realistic synoptic-scale conditions. Additional model configuration choices include the Noah-MP (Niu et al. 2011); the RRTM for GCMs (RRTMG) radiation scheme (Iacono et al. 2008); the Grell–Freitas cumulus parameterization

[1] Vertical levels are unequally spaced with higher vertical resolution near the surface and near the model top.

on the 36-, 12-, and 4-km domains (Grell and Freitas 2014); Thompson microphysics (Thompson et al. 2008); and the Yonsei University boundary layer scheme (Hong et al. 2006). Following Barnes et al. (2018), the NCEP North American Regional Reanalysis (NARR; Mesinger et al. 2006) was used to evaluate the simulated synoptic conditions for the two case studies.

Figure 2 presents a map of the OLYMPEX observing locations used in this study and the regional terrain. Barnes et al. (2018) and Houze et al. (2017) described the OLYMPEX instrumentation used to observe KH waves, including the NASA polarimetric (NPOL) radar near the Washington coast (149 m ASL). Data from two OLYMPEX surface stations are used in this paper: the Fishery (52 m ASL) and Bishop Field (87 m ASL) sites; both included rain gauges and Parsivel disdrometers to document particle sizes.

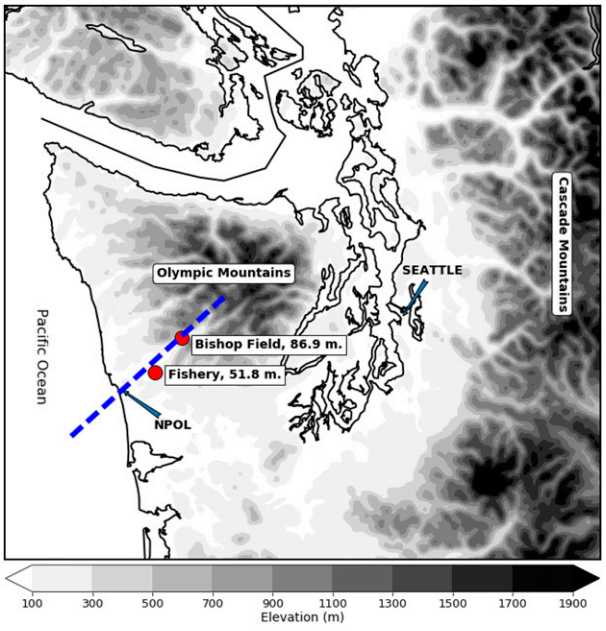


FIG. 2. Regional terrain (shaded), major geographical features, and the OLYMPEX observing stations used in this study. The dashed blue line indicates the location of the vertical cross section applied in this study.

## 3. Case 1: 12 December 2015

### a. *Observed and simulated mesoscale conditions and wave generation*

The first event on 12 December 2015 was characterized by a midlatitude cyclone that approached from the west. At 1200 UTC 12 December 2015, prior to the period of observed KH waves, NARR showed a 925-hPa low with strong low-level winds [50 kt (25 m s$^{-1}$)] off the British Columbia coast (Fig. 3a). Such strong low-level flow supported wave development, enhancing the low-level wind shear in which the observed waves formed. Although WRF realistically captured the position and timing of the system (Fig. 3b), the simulated low center was deeper than observed by 80 m, with 925-hPa wind speeds that were modestly stronger [5 kt (2.5 m s$^{-1}$)] than observed. The 444-m simulated vertical profile during the period of KH waves (2135 UTC; Fig. 3d) was consistent with observations at the NPOL radar (Fig. 3c), including a stable saturated layer below 700 hPa and substantial wind shear below 900 hPa. The observed dry layer at ~2.8 km was less pronounced in WRF, though as described below, simulated and observed waves rarely reach this altitude, and thus, the effects on wave development would be expected to be minimal.

Figure 4 displays the Doppler on Wheels (DOW) radar observations from Barnes et al. (2018), which documented KH waves within the melting level of stratiform precipitation in the vicinity of Bishop Field on 12 December. Waves were observed in the 1–3 km AGL layer, with perturbations most pronounced in the reflectivity and velocity fields. The waves had a wavelength of ~5 km and a period of ~7 min.

The Richardson number (Ri) is a common diagnostic for KH waves, with waves developing when Ri $<$ 0.25 (Miles and Howard 1964) and Ri $<$ 1 being sufficient for wave maintenance once initiated (Weckwerth and Wakimoto 1992). Here, we define Ri using the moist Brunt–Väisälä frequency (Lalas and Einaudi 1974) in a saturated environment and the dry Brunt–Väisälä frequency when unsaturated. Model vertical cross sections showed a decrease in Ri below 2 km prior to the onset of simulated waves around 1800 UTC (Fig. 5a). At 0900 UTC, a thin layer of Ri $<$ 1 was noted around 500 m ASL; by 1200 UTC, this layer had grown considerably in magnitude but not in depth, with critical ($<$0.25) values noted over Bishop Field. Beginning around 1800 UTC, wave structures appeared in the 0.5–1-km layer and progressively grew in the vertical, with some approaching 2.5 km ASL by 2100 UTC over Bishop Field. Such vertical expansion was noted in observations by Barnes et al. (2018), with the waves appearing to perturb the melting level between Fishery and Bishop at the final time. Because Ri reflects the ratio of atmospheric stability to vertical wind shear, the atmosphere must become less stable and/or vertical shear must increase to obtain critical values of Ri. Both of these factors contributed to wave development/maintenance in this case (Figs. 5b,c), although increasing shear was dominant, a situation that has been observed over the Sierra Nevada (Medina and Houze 2016).

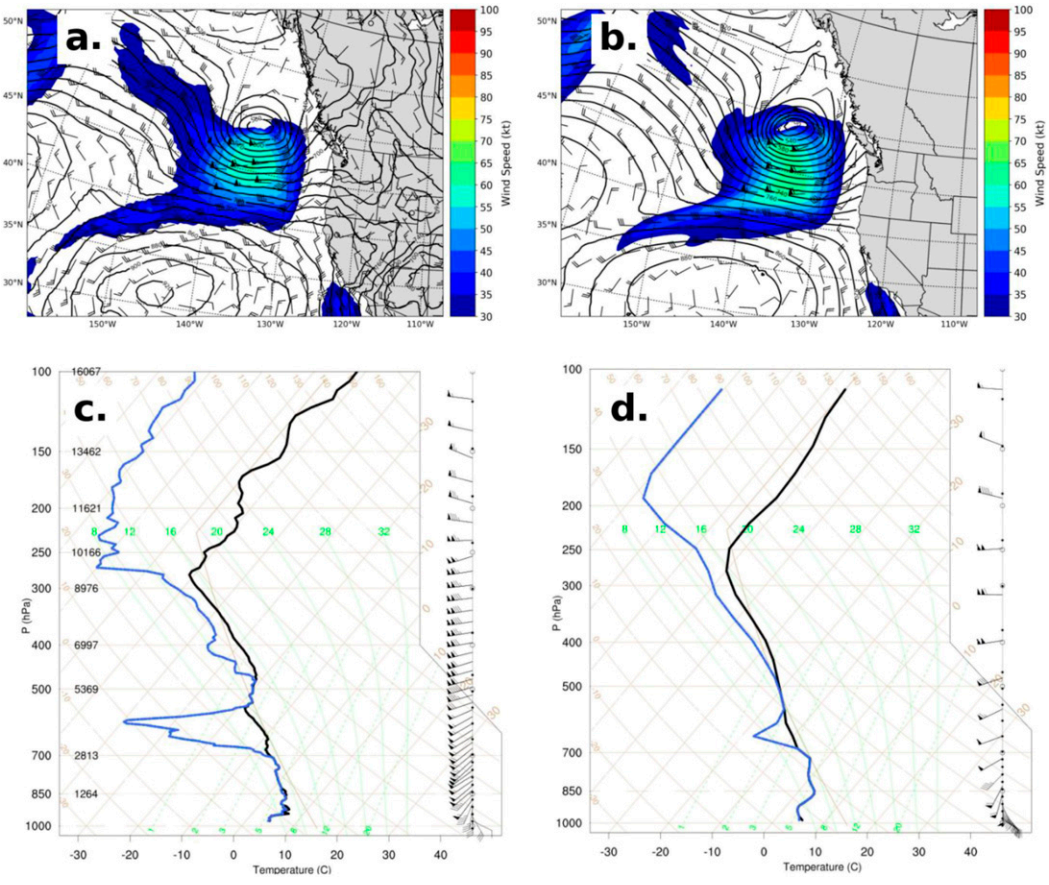


FIG. 3. (a) NARR and (b) WRF geopotential heights (black contours; 20-m interval), wind barbs, and wind speed (shading) at 925 hPa for the 36-km domain valid at 1200 UTC 12 Dec 2015. (c) Observed and (d) 444-m simulated soundings at the NPOL site, valid at ~2135 UTC 12 Dec 2015.Wind barbs in (d) are plotted at standard meteorological levels.

Figure 5b shows the evolution of simulated vertical wind shear during this event. Initially, vertical shear was greatest over land because of surface drag, but subsequently, the layer of large shear in the lower troposphere strengthened and expanded vertically between 0900 and 1800 UTC, as low-level easterly flow developed beneath westerly flow aloft. Environmental stability (shown here as the vertical gradient in potential temperature, a metric well suited to show wave overturning) decreased near the surface prior to wave generation (Fig. 5c) as the front approached. The appearance of waves around 1800 UTC coincided with the decrease in low-level stability between Bishop and Fishery. Overturning waves were evident in cross sections of $d\theta/dz$, evinced by unstable lapse rates at 2100 UTC near and upstream of Bishop.

The appearance of KH waves in the simulation was highly sensitive to horizontal grid spacing. Figure 6 shows radial winds along the cross section at 2100 UTC from the NPOL radar and WRF at various horizontal grid spacings. In all domains, WRF was able to reproduce observed mesoscale conditions, including the transition at approximately 1 km AGL from low-level easterly flow to westerly flow aloft. No wave activity was evident using 4-km grid spacing, and only weak waves were noted in the 1.33-km domain. Only at 444-m grid spacing did the KH waves have realistic amplitudes and wavelengths (e.g., a wavelength of ~3.1 km at 2 km AGL). Such dependence on grid spacing follows from basic principles, since the effective resolution of WRF is roughly 6 times the grid spacing (Skamarock 2004; Skamarock et al. 2014), which would be 2.6 km for 444-m grid spacing and 7.8 km for the 1.3-km domain. Thus, only the 444-m domain had sufficient resolution to adequately resolve the observed KH waves, which had observed wavelengths of 4–5 km (Barnes et al. 2018).

The simulated KH structures were most prominent immediately upstream of and over the Olympic foothills, with some wave activity up to ~40 km offshore,

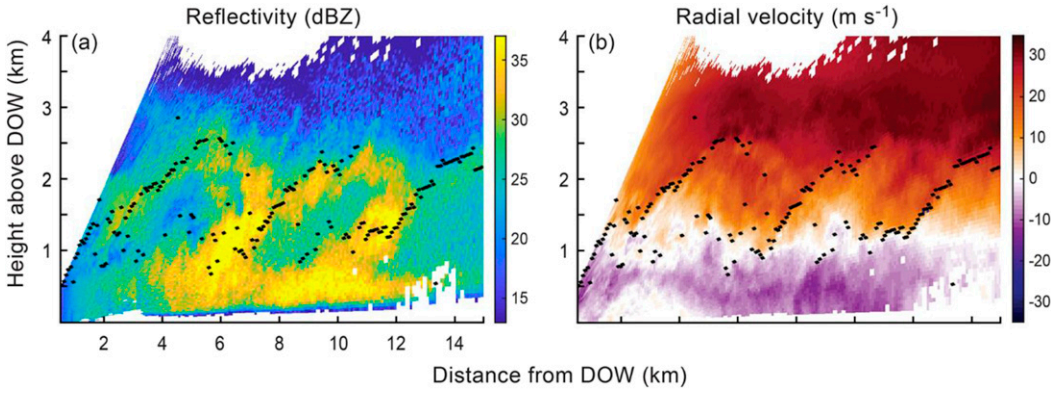


FIG. 4. (a) Reflectivity (dB$Z$) and (b) radial velocity (m s$^{-1}$) from an RHI scan of the DOW radar at an azimuthal angle of 54° at 2110 UTC 12 Dec 2015. The black dots show the location of the maximum spectrum width in each vertical column [based on Fig. 9 in Barnes et al. (2018); used with permission].

where low-level wind shear increased as incoming flow was blocked by the Olympic Mountains (Fig. 6d). Furthermore, waves weakened after traversing higher terrain over the eastern portion of the domain.

To evaluate the impact of terrain blockage on the development of KH waves during this event, the Olympics were removed in an additional WRF simulation (Fig. 7b) while retaining the changes in surface characteristics between water and land. For the 12 December event, removing the mountains greatly lessened the low-level flow deceleration, eliminated the low-level easterly flow at the surface, and greatly reduced the low-level shear. Some small-amplitude oscillations remained over western portions of the cross section, resulting from localized ascent along the occluded front. Thus, it appears that orography was necessary for the development of KH waves in this case.

### b. *Impact of KH waves on microphysics*

Analyzing polarimetric radar data, Barnes et al. (2018) found that the observed KH waves during the

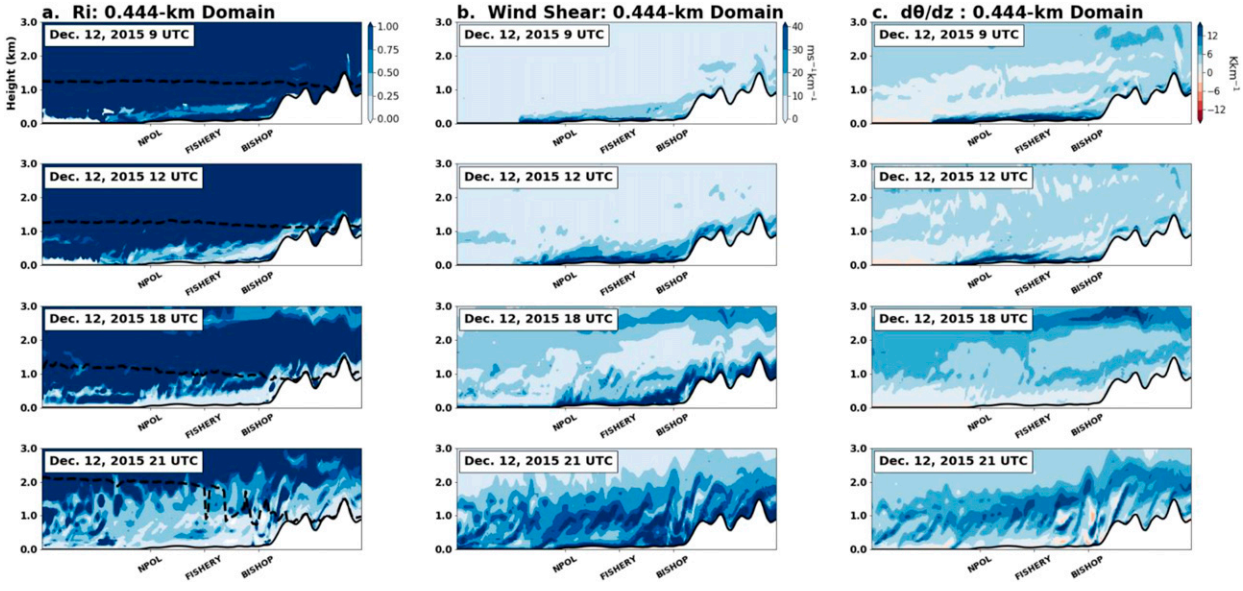


FIG. 5. Vertical cross sections of (a) Richardson number, (b) vertical wind shear, and (c) stability ($d\theta/dz$) along the cross section in Fig. 2 at various stages of the 12 Dec 2015 event. The 444-m domain fields are shown. The dashed line in (a) is the melting level.

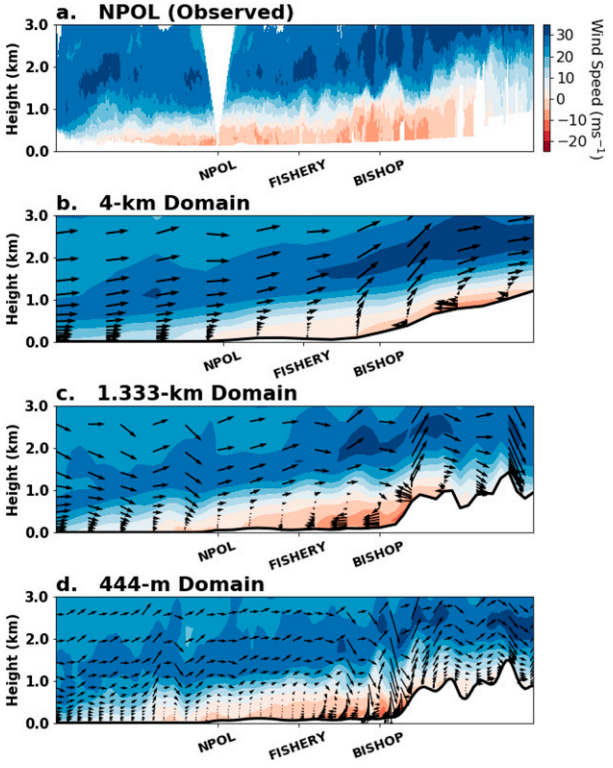


FIG. 6. Vertical cross sections of (a) NPOL radar-based, (b) 4-km, (c) 1.33-km, and (d) 444-m simulated radial winds along the cross section shown in Fig. 2, valid at 2100 UTC 12 Dec 2015. Note that the Pacific coast is located just west of NPOL.

12 December event influenced microphysics, particularly when the waves were near the melting level. Specifically, enhanced reflectivity and turbulence (spectral width) within the upward branch of the waves were associated with greater riming. The impact of simulated KH waves on model microphysics in the 444-m domain is explored below.

At Bishop Field, where waves were observed in Barnes et al. (2018), simulated vertical velocity and microphysical quantities showed wavelike variability from 2000 to 2300 UTC (Fig. 8): Simulated vertical velocity oscillations exceeded 5 m s$^{-1}$ within the 0.5–3-km layer, which impacted surface mass-weighted mean drop diameter $\overline{D_{\mathrm{mw}}}$ and mixing ratios of cloud and rainwater. Precipitation in the 444-m domain was modulated by the waves, albeit with a smaller amplitude than observed.

Vertical cross sections in the Quinault valley from the NPOL site to Bishop Field, taken at 2010 UTC, are presented in Fig. 9. These cross sections show that simulated reflectivity, $\overline{D_{\mathrm{mw}}}$, and rain number concentration were modulated by the waves, with enhancements immediately downstream of local vertical velocity maxima. Enhancement and wavelike modulation of reflectivity (dB$Z$) were found in the lowest 2 km of the simulation, with particularly large values just below the melting level.

## 4. Case 2: 17 December 2015

### a. Observed and simulated mesoscale conditions

During the second event on 17 December 2015, KH waves were observed for 6 h (1200–1800 UTC) over the Quinault valley (Barnes et al. 2018). At 0600 UTC, the NARR analyzed a 925-hPa low over the Gulf of Alaska, with an occluded front extending southward offshore of the coast of Washington State, and strong [>40 kt (>20.58 m s$^{-1}$)] winds along and north of the front (Fig. 10a). The synoptic conditions of this event were well simulated by WRF, although the simulated low was slightly deeper, with low-level winds stronger than observed (Fig. 10b). The simulated frontal position agreed with NARR, and simulated and observed vertical profiles at the NPOL site were in good agreement at the beginning of the event (1430 UTC; Figs. 10c,d). Specifically, WRF accurately simulated moist neutral conditions above 700 hPa, a stable layer below the melting level, and vertical wind shear exceeding 40 m s$^{-1}$ below 1.5 km.

Radar observations in Barnes et al. (2018) for this event (reproduced in Fig. 11) showed KH waves offshore and throughout the valley below 1.5 km, which was beneath the observed melting level (2.5 km). Observed waves had a wavelength of 4–5 km and period of ~10 min. These waves were found in the 0.5–1.5-km layer and had a smaller vertical extent than the 12 December event. Radar vertical cross sections indicated that waves amplified as they approached the Olympic Mountains (Fig. 14 in Barnes et al. 2018). In the 444-m simulation, KH waves occurred between 0.5 and 2 km, with the greatest amplitudes within a layer of vertical shear between low-level easterly flow and westerly flow aloft (Fig. 12). This shear layer was evident at 1200 UTC in both the NPOL radial winds and in the 444-m simulation. Simulated waves had a 3-km wavelength and a period of 17 min.

Wave onset coincided with Ri declining to criticality (below 0.25) around 1200 UTC within the low-level shear layer. Figure 13a shows cross sections of Ri before and during the wave event. At 0500 UTC, Ri was less than 0.5 in the lowest 300 m ASL, with some wavelike perturbations approximately 100 m above the coastal ocean. Between 0500 and 0800 UTC, Ri and vertical shear (Fig. 13b) were relatively unchanged at low levels, with little evidence of the growth of KH waves as the low-level flow became more stable. Only aloft

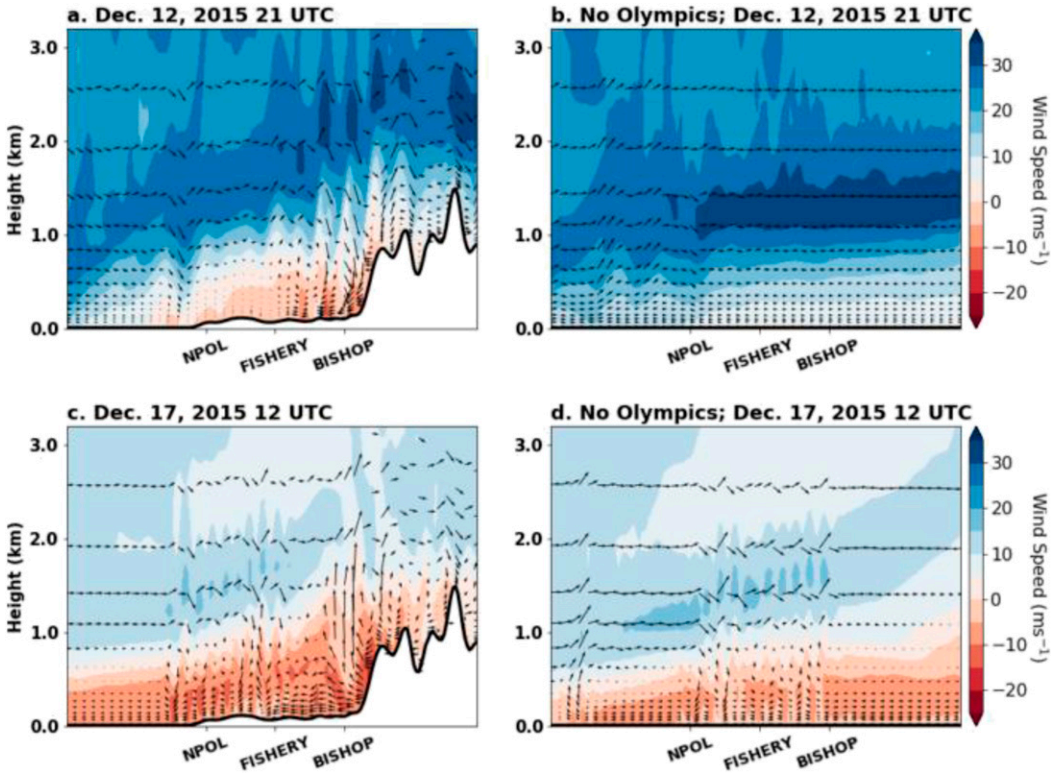


FIG. 7. Vertical cross sections of (a) 444-m simulated radial winds along the cross section in Fig. 2, valid at 2100 UTC 12 Dec 2015; (b) simulation without the Olympic Mountains. (c),(d) As in (a) and (b), respectively, but valid at 1200 UTC 17 Dec 2015.

(2 km ASL) was shear increasing. At 1200 UTC, the front had passed the Fishery site with a dramatic increase in wind shear below 2 km and KH waves appearing between 0.5 and 1.5 km (Fig. 13c). By 1500 UTC, the layer of strong vertical wind shear thinned, and wave amplitude began to decline (Fig. 13d). Thus, it appears that KH waves in this case were initiated by the increasing wind shear associated with the approaching front.

As in the 12 December case, waves expanded vertically as they approached terrain. At 1200 UTC, waves near the coastal NPOL site were evident in a layer approximately 500 m deep and increased to 1 km in vertical extent over Fishery, with lessened wave activity over higher terrain. Unlike the first case, however, removal of the Olympic Mountains did not eliminate the easterly surface flow (Fig. 7d), and some wave activity remained without terrain, confirming that the primary cause of the KH waves during this event was the synoptic environment and not terrain blocking.

### b. *Impact of KH waves on microphysics*

Vertical velocity modulations associated with the KH waves had less impact on model microphysics than in the 12 December case, likely because waves were weaker and occurred below the melting level. Figure 14 shows cross sections between the NPOL and Bishop sites at 1320 UTC, when Barnes et al. (2018) observed KH waves in the vicinity. While there were modest modulations in vertical velocity, $\overline{D_{\mathrm{mw}}}$, simulated reflectivity, and rain number concentration, the amplitudes were considerably weaker than during the previous event.

Turning to the observations and model output at the Fishery site, there are modest modulations between 1300 and 1800 UTC of several observed microphysical quantities and the precipitation rate (0.3 mm h$^{-1}$), with periods similar to the observed waves (Barnes et al. 2018). Simulated mixing ratios at the Fishery site showed minor variations in rain, cloud water, and snow during the same period, with little graupel present (Fig. 15a). Simulated vertical velocities oscillated with an amplitude of ~1 m s$^{-1}$ (Fig. 15b), several meters per second less than observations from vertically pointing radar. In contrast to the 12 December case, time series of simulated precipitation rates and $\overline{D_{\mathrm{mw}}}$ showed less influence from KH waves during this event (Figs. 15c,d).

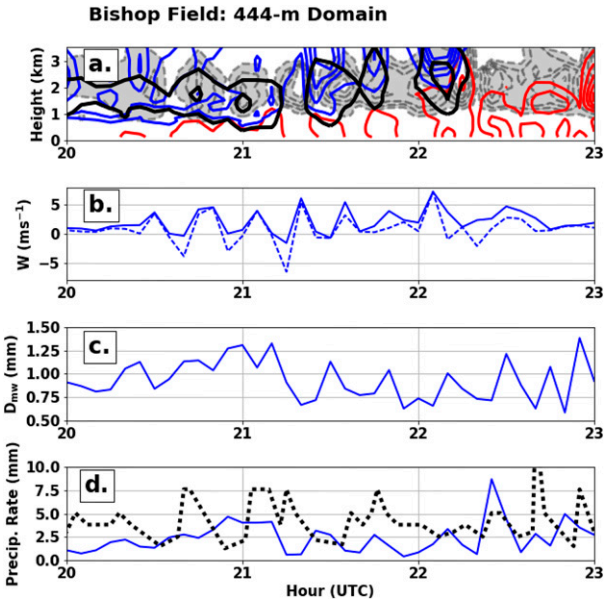


FIG. 8. Simulated vertical profiles at Bishop Field for 2000–2300 UTC of (a) cloud water mixing ratio (gray fill; gray dashed contours), rainwater mixing ratio (red), graupel mixing ratio (black), and snow mixing ratio (blue); (b) 2.0-km vertical velocity (solid) and 0.5–3-km maximum vertical velocity (dashed); (c) mass-weighted mean raindrop diameter at the lowest model height; and (d) simulated (solid) and observed precipitation rate (dashed).

## 5. Impact of choice of microphysical parameterizations

Simulated microphysical quantities were modulated by KH waves, and thus, it is important to determine the sensitivity of KH waves to the choice of microphysical parameterizations. For microphysics experiments, we applied the Morrison double-moment scheme[2] (MORR2; Morrison and Milbrandt 2011), the Thompson et al. (2008) scheme, and WSM6[3] (Hong and Lim 2006). The control run, used in the simulations described in section 2, consisted of Thompson microphysics and Yonsei University (YSU) PBL. A dry run using YSU PBL, with no microphysics or latent heating, was also completed. Table 1 outlines the model experiments completed for this section.

### a. *Case 1: 12 December 2015*

The removal of moist physics and latent heating from the model produced a substantial difference between

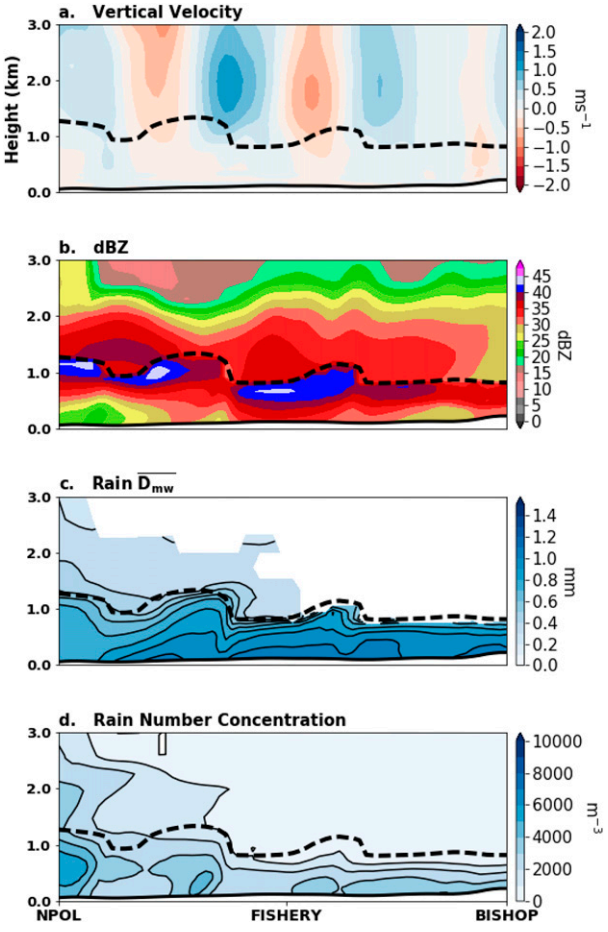


FIG. 9. Vertical cross section from NPOL to Bishop Field along the cross section in Fig. 2 of simulated (a) vertical velocity, (b) reflectivity, (c) mass-weighted mean raindrop diameter, and (d) rain number concentration at 2010 UTC 12 Dec. The dashed line is the melting level.

the wave activity of the control and dry runs for the 12 December 2015 case, when waves were impacting the melting level. At the Fishery site, the control simulation had vertical velocity amplitudes associated with KH waves in excess of 2 m s$^{-1}$ (Fig. 16). In contrast, there was no wave activity in the dry run, with only minor oscillations of less than 0.5 m s$^{-1}$. At Bishop Field, wave amplitudes were large in the control simulation between 2000 and 2200 UTC, while in the dry run, the waves were attenuated after 2100 UTC. The results of the dry runs for both cases are consistent with the findings of Kudo (2013), who showed that latent heat can reduce stability, providing more favorable conditions for the waves. The period of the waves in the dry run was greater (22 min) than that of the control run and with a longer wavelength (5 km compared to 3 km).

Varying microphysics schemes had a significant impact at both sites for this event. Figure 17a shows

[2] The Morrison double-moment microphysics schemes uses double-moment formulations for all hydrometeor species, which makes it preferable over other double-moment schemes for assessing the impact of hydrometeors on KH waves.

[3] WSM6 was chosen because of its tendency to produce excessive graupel (e.g., Grasso et al. 2014; Han et al. 2013), which could potentially impact vertical velocity from hydrometeor loading.

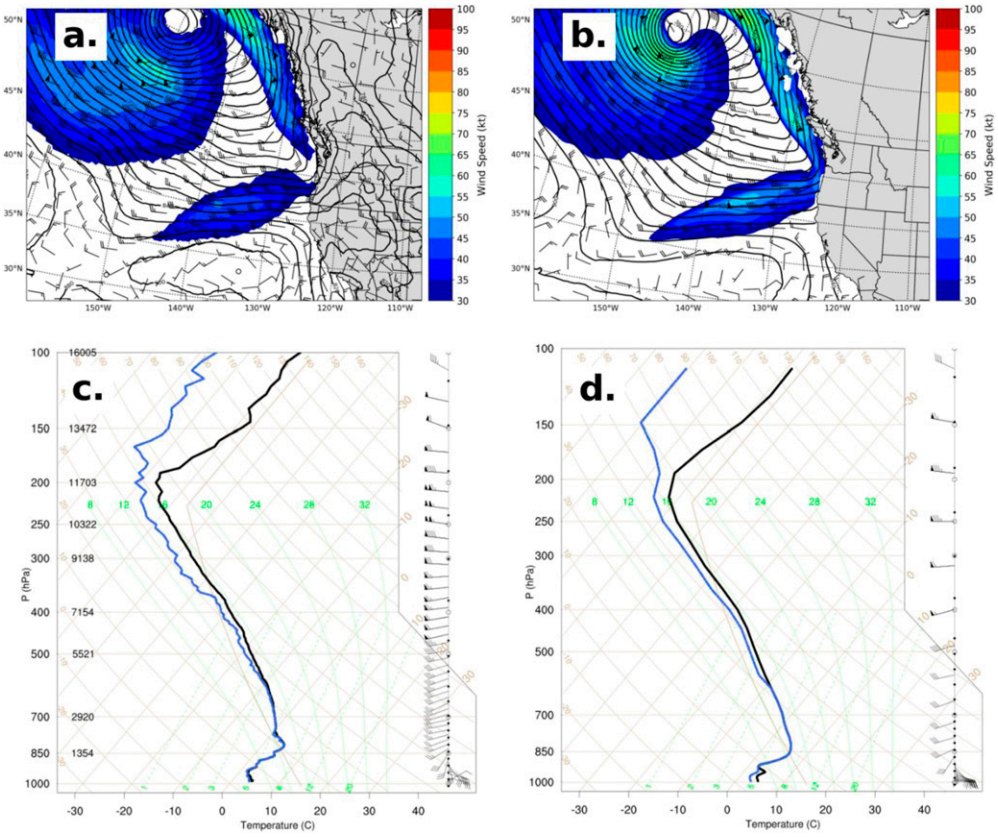


FIG. 10. (a) NARR and (b) WRF 925-hPa geopotential heights (black contours; 20-m contour interval), wind barbs (kt), and wind speed (shading) for the 36-km domain, valid at 0600 UTC 17 Dec 2015. (c) Observed and (d) 444-m simulated soundings at the NPOL site, valid at ~1430 UTC 17 Dec 2015.

time-averaged values for 1900–2300 UTC of vertical velocity and mixing ratios. Examining the impact of various microphysics schemes at Fishery, vertical motion was reduced in the Morrison and WSM6 schemes compared to the control run, with a coincident increase in graupel mixing ratios in both schemes, which is consistent with decreased updraft speeds due to hydrometeor loading and graupel generation. Furthermore,

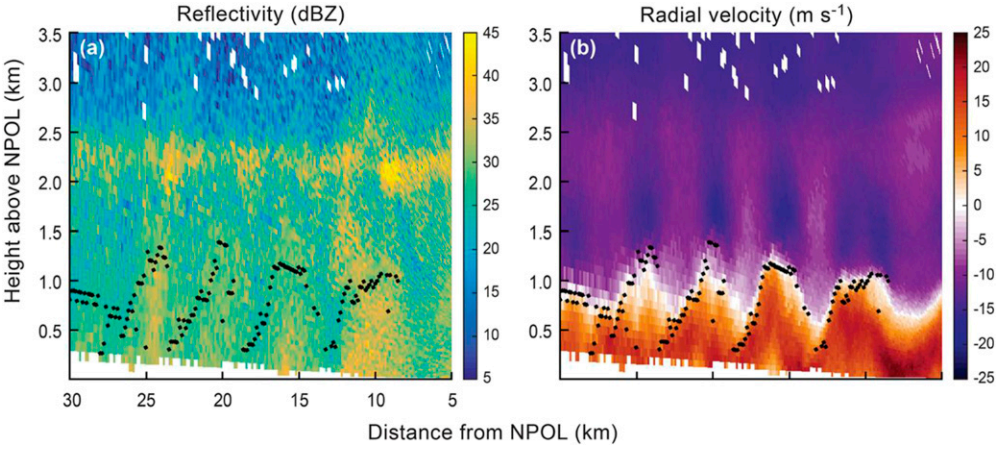


FIG. 11. (a) Reflectivity (dB$Z$) and (b) radial velocity (m s$^{-1}$) from an RHI scan from the NPOL radar at an azimuthal angle of 254° at 1320 UTC 17 Dec 2015. The black dots show the location of the maximum spectrum width in each vertical column [based on Fig. 10 in Barnes et al. (2018); used with permission].

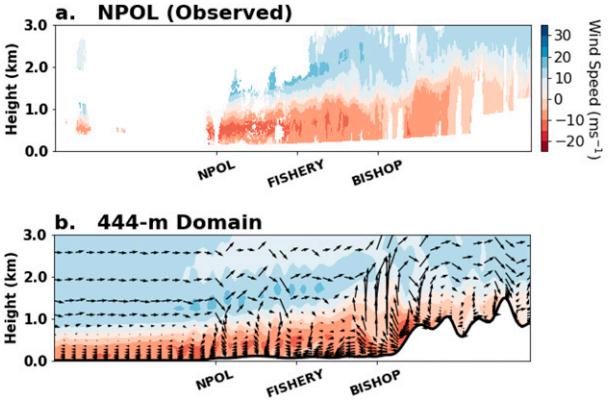


FIG. 12. Vertical cross sections of (a) observed and (b) 444-m simulated radial wind extending northeast along the cross section in Fig. 2, valid at 1200 UTC 17 Dec 2015.

cloud water mixing ratios are larger than rainwater or graupel mixing ratios at both sites, which is indicative of the introduction or generation of supercooled liquid water in the vicinity of the freezing level.

### b. *Case 2: 17 December 2015*

In the 17 December 2015 case, when the KH waves were located below the melting level, the removal of moist physics resulted in a small decline in vertical velocity compared to the control run (Fig. 16). At Fishery, the dry run had only intermittent vertical velocity modulations of less than 1 m s$^{-1}$, somewhat weaker than those of the control run during the 1200–1800 UTC period. At Bishop Field, wave activity appeared in both simulations, without any consistent difference in amplitudes. The period of waves in the dry run was 17 min with a wavelength of 3.3 km, similar to those found in the control simulation. Varying model physics produced notable differences (Fig. 17b). All schemes showed little graupel or cloud water, which is logical because waves were below the melting level, while the Morrison and WSM6 schemes reduced rainwater mixing ratios compared to the control run.

## 6. Discussion and conclusions

Kelvin–Helmholtz (KH) waves observed during two events of the OLYMPEX field campaign were simulated and examined in this work. The events, 12 and 17 December 2015, possessed similar synoptic conditions, with an occluded front approaching Washington State from the west. The WRF Model accurately simulated the observed synoptic and mesoscale environments of these events and development of KH waves over the western side of the Olympic Mountains.

During the 12 December case, KH waves were observed within the melting level in the Quinault valley of the Olympic Mountains of Washington State. Simulated cross sections indicated KH waves in the same region, with modeled wave structures agreeing qualitatively with radar observations from Barnes et al. (2018), including the altitude and vertical extent of the waves. Because of the observed 3–5-km wavelengths, the ability

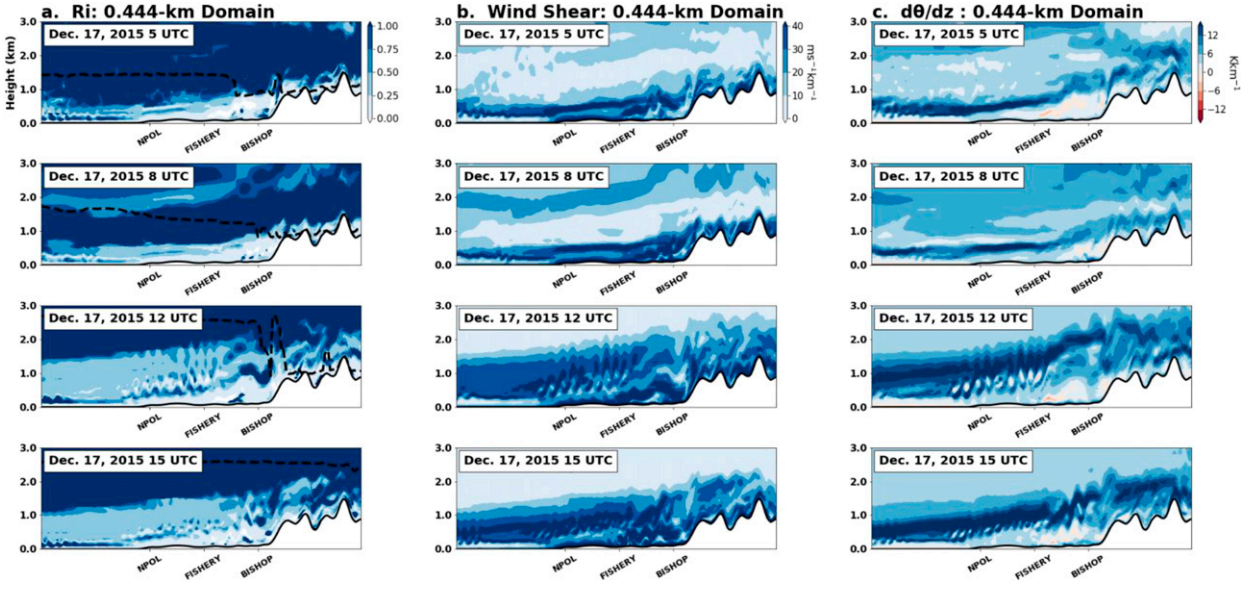


FIG. 13. Vertical cross sections of (a) Richardson number, (b) vertical wind shear, and (c) $d\theta/dz$ along the cross section in Fig. 2 at various stages of the 17 Dec 2015 event. The dashed line in (a) is the melting level.

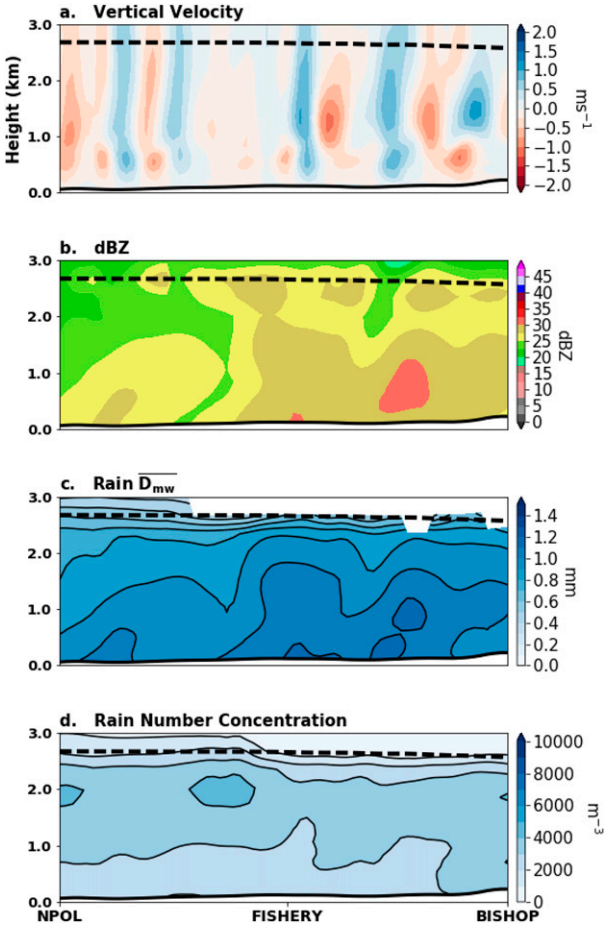


FIG. 14. Simulated vertical cross section from the NPOL site to Bishop along the line in Fig. 2 of (a) vertical velocity, (b) reflectivity, (c) mass-weighted mean raindrop diameter, and (d) rain number concentration at 1320 UTC 17 Dec. The dashed line is the melting level.

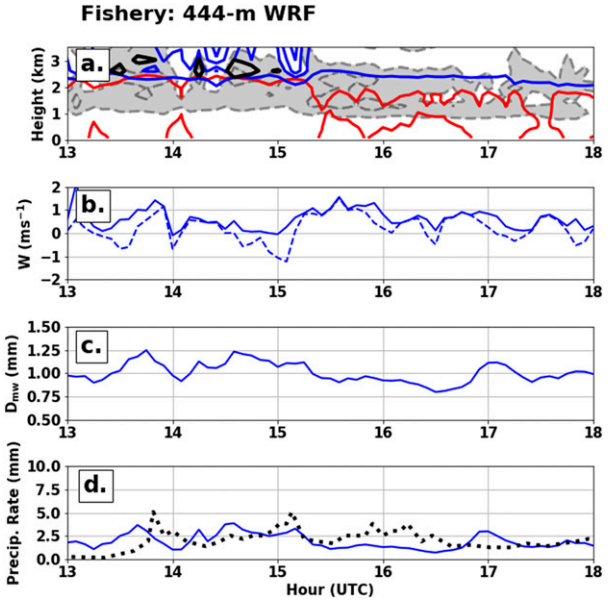


FIG. 15. Simulated vertical profiles at the Fishery site for 1300–1800 UTC of (a) cloud water mixing ratio (gray fill; gray dashed contours), rainwater mixing ratio (red), graupel mixing ratio (black), and snow mixing ratio (blue); (b) 0.5-km vertical velocity (solid) and 0.5–3-km maximum vertical velocity (dashed); (c) mass-weighted mean raindrop diameter at the lowest model height; and (d) simulated (solid) and observed (dashed) precipitation rate.

to simulate the waves was resolution dependent: only at 444-m grid spacing were the waves adequately resolved despite the 4-km domain being able to simulate the synoptic and mesoscale environment around the barrier. Simulated KH waves developed as the Richardson number on the southwest side of the Olympics dropped to approximately 0.25. The decline in Richardson number had two origins: the strengthening of easterly flow near the surface, causing wind shear to increase, and a concomitant reduction of low-level stability.

The 17 December event had observed and simulated KH waves below the melting level in the Quinault valley. As in the earlier event, simulated wave structures agreed with radar observations, and development was driven by increasing vertical shear and decreasing stability. Simulated waves during these events were consistent with KH waves and not with internal gravity waves for several reasons: 1) potential temperature and horizontal wind perturbations were in phase, which is a configuration not found with internal gravity waves; 2) overturning of waves was evident; and 3) waves formed in a region of strong vertical wind shear and met the critical Richardson number criterion.

The Olympic Mountains played a critical role during the 12 December event by blocking the incoming flow and producing low-level easterly winds, which in turn contributed to increased vertical wind shear, a lowered Richardson number, and resulting KH waves. Removing the Olympics prevented development of easterly near-surface flow, thereby eliminating the shear zone and resulting in the absence of wave development. In contrast, during the 17 December event, low-level easterly flow was synoptically forced and began hours prior to wave onset. Removing the Olympics reduced, but did not eliminate, the low-level easterly winds, and KH waves still developed within a shear layer.

The impact of the simulated KH waves on microphysics agreed with conceptual models presented in Houser and Bluestein (2011) and Barnes et al. (2018). Barnes et al. (2018) found that riming and aggregation were modulated by KH waves within or above the melting level. For the 12 December event, the simulation showed collocated enhancement of vertical velocity, snow and graupel mixing ratios, and mass-weighted

TABLE 1. Physics experiments that were conducted for both cases.

| Experiment name | Microphysics | PBL | Latent heat |
|---|---|---|---|
| Control run | Thompson | YSU | On |
| WSM6 | WSM6 | YSU | On |
| MORR2 | Morrison double moment | YSU | On |
| Dry run | None | YSU | Off |

mean drop diameter $\overline{D_{mw}}$ by the wave circulations. Enhancements in cloud water mixing ratios were collocated with upward motion in the waves and was largest in the vicinity of and immediately above the melting level, which is consistent with generation of supercooled water necessary for riming. Thus, it appears that wave activity enhanced riming and aggregation, which grew particles that melted as they fell below the melting level, resulting in larger raindrop sizes below the waves.

During the 17 December event, KH waves occurred below the melting level. In this regime, the Barnes et al. (2018) conceptual model indicates coalescence and vapor deposition as the primary microphysical processes occurring within and above the waves. These processes are slower to grow particles than aggregation or riming; thus, little snow or graupel was simulated during the wave period, and the majority of cloud water enhancement occurred below the melting level. In the simulation, rain number concentration was enhanced in the 1–2 km AGL layer, and $\overline{D_{mw}}$ increased closer to the surface. Cloud water coalesced and grew into rain droplets above the KH waves, leading to larger rain number concentrations. Subsequently, these raindrops fell, continuing their collision–coalescence until impacting the surface.

Oscillations in precipitation at Bishop Field were present in both observations and simulations for the 12 December event. In contrast, when KH waves were below the melting level (17 December), there was little modulation of observed or simulated precipitation.

Finally, the impact of varying microphysical parameterizations was evaluated for each event. Turning off microphysics and latent heating in the simulations weakened vertical velocities in the waves compared to the control run for both cases. Graupel and cloud water mixing ratios were more dependent on scheme selection during the 12 December event than the 17 December event, and 17 December had greater rainwater mixing ratios.

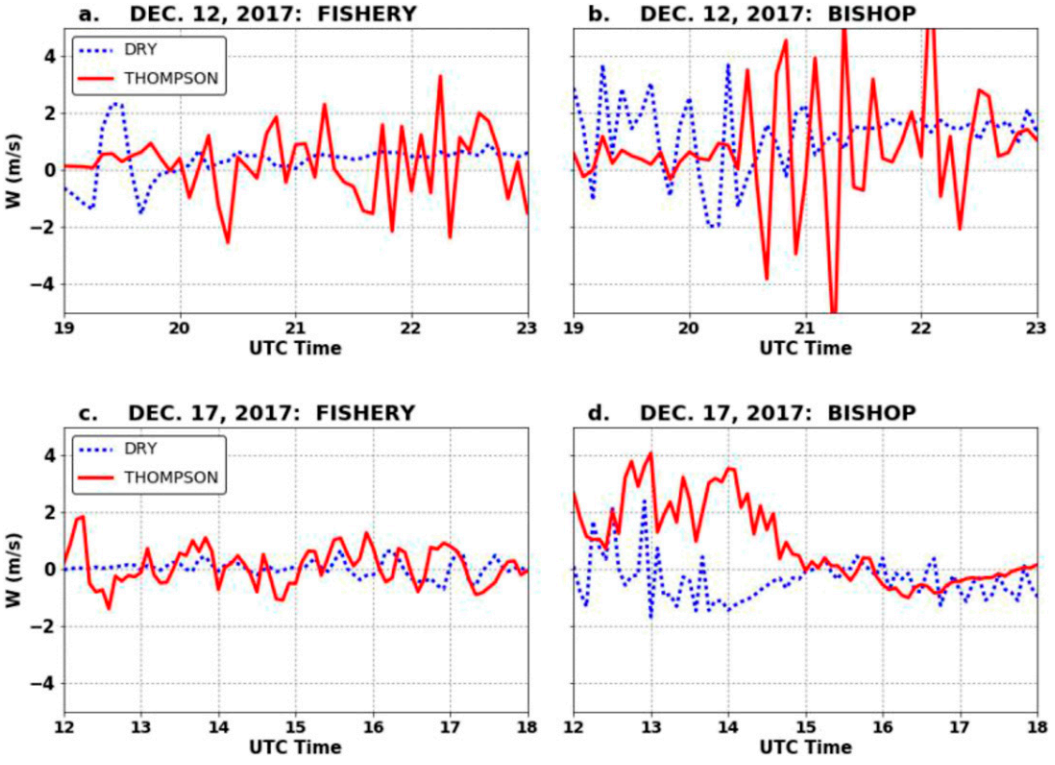


FIG. 16. Time series of 2-km vertical velocity during the period 1900–2300 UTC 12 Dec 2015 at (a) Fishery and (b) Bishop Field and 1-km vertical velocity during the period 1200–1800 UTC 17 Dec 2015 at (c) Fishery and (d) Bishop. All plots show the dry and control (Thompson) simulations.

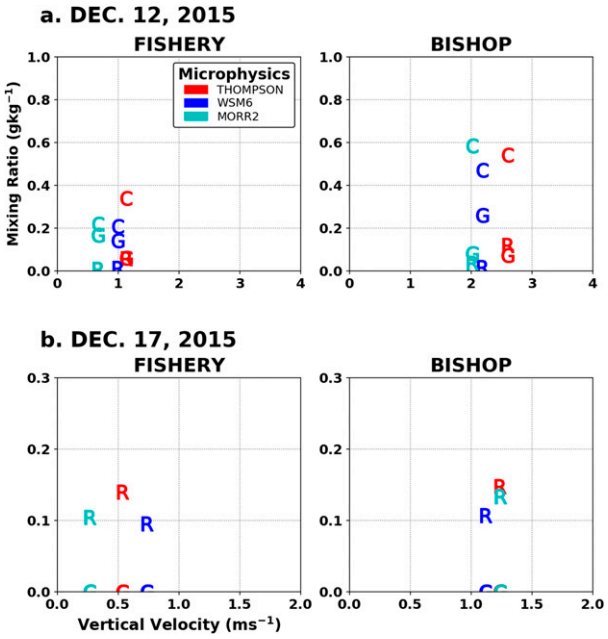


FIG. 17. Time-average quantities of mixing ratios [rain (R), graupel (G), and cloud water (C)] and vertical velocity from all microphysics experiments at (a) 2 km during 1900–2300 UTC 12 Dec 2015 at Fishery and Bishop Field and (b) 0.5 km during 1200–1800 UTC 17 Dec 2015. All quantities are average values at times when the vertical velocity at 2 or 0.5 km, respectively, is locally maximized.

In summary, this study has found that Kelvin–Helmholtz waves and the environmental conditions conducive to their development can be accurately reproduced in WRF simulations but only at sufficiently fine grid spacing. Furthermore, the simulated waves did influence model microphysics and precipitation. Future work will focus on describing, quantifying, and evaluating the simulated microphysical processes that operate in simulated waves.

*Acknowledgments.* This research was supported by the National Science Foundation through Grant AGS-1349847. The authors would also like to thank three anonymous reviewers for their comments and suggestions, as well as Hannah Barnes, Robert Houze, Lynn McMurdie, and Joe Zagrodnik for the productive discussions and allowing use of some figures.

## REFERENCES

Barnes, H. C., J. P. Zagrodnik, L. A. McMurdie, A. K. Rowe, and R. A. Houze Jr., 2018: Kelvin–Helmholtz waves in precipitating stratiform clouds of midlatitude baroclinic cyclones. *J. Atmos. Sci.*, https://doi.org/10.1175/JAS-D-17-0365.1, in press.

Browning, K. A., J. H. Marsham, B. A. White, and J. C. Nicol, 2012: A case study of a large patch of billows surmounted by elevated convection. *Quart. J. Roy. Meteor. Soc.*, **138**, 1764–1773, https://doi.org/10.1002/qj.1908.

Droegemeier, K. K., and R. B. Wilhelmson, 1987: Numerical simulation of thunderstorm outflow dynamics. Part I: Outflow sensitivity experiments and turbulence dynamics. *J. Atmos. Sci.*, **44**, 1180–1210, https://doi.org/10.1175/1520-0469(1987)044<1180:NSOTOD>2.0.CO;2.

Efimov, V. V., 2017: Numerical simulation of breeze circulation over the Crimean Peninsula. *Atmos. Oceanic Phys.*, **53**, 84–94, https://doi.org/10.1134/S0001433817010042.

Friedrich, K., D. E. Kingsmill, C. Flamant, H. V. Murphy, and R. M. Wakimoto, 2008: Kinematic and moisture characteristics of a nonprecipitating cold front observed during IHOP. Part II: Alongfront structures. *Mon. Wea. Rev.*, **136**, 3796–3797, https://doi.org/10.1175/2008MWR2360.1.

Fritts, D. C., 1979: The excitation of radiating waves and Kelvin-Helmholtz instabilities by the gravity wave-critical level interaction. *J. Atmos. Sci.*, **36**, 12–23, https://doi.org/10.1175/1520-0469(1979)036<0012:TEORWA>2.0.CO;2.

——, T. L. Palmer, Ø. Andreassen, and I. Lie, 1996: Evolution and breakdown of Kelvin–Helmholtz billows in stratified compressible flows. Part I: Comparison of two- and three-dimensional flows. *J. Atmos. Sci.*, **53**, 3173–3191, https://doi.org/10.1175/1520-0469(1996)053<3173:EABOKB>2.0.CO;2.

Geerts, B., and Q. Miao, 2010: Vertically pointing airborne Doppler radar observations of Kelvin–Helmholtz billows. *Mon. Wea. Rev.*, **138**, 982–986, https://doi.org/10.1175/2009MWR3212.1.

Grasso, L., D. T. Lindsey, K. S. Lim, A. Clark, D. Bikos, and S. R. Dembek, 2014: Evaluation of and suggested improvements to the WSM6 microphysics in WRF-ARW using synthetic and observed *GOES-13* imagery. *Mon. Wea. Rev.*, **142**, 3635–3650, https://doi.org/10.1175/MWR-D-14-00005.1.

Grell, G. A., and S. R. Freitas, 2014: A scale and aerosol aware stochastic convective parameterization for weather and air quality modeling. *Atmos. Chem. Phys.*, **14**, 5233–5250, https://doi.org/10.5194/acp-14-5233-2014.

Han, M., S. A. Braun, T. Matsui, and C. R. Williams, 2013: Evaluation of cloud microphysics schemes in simulations of a winter storm using radar and radiometer measurements. *J. Geophys. Res. Atmos.*, **118**, 1401–1419, https://doi.org/10.1002/jgrd.50115.

Hong, S.-Y., and J.-O. J. Lim, 2006: The WRF single-moment 6-class microphysics scheme (WSM6). *J. Korean Meteor. Soc.*, **42**, 129–151.

——, Y. Noh, and J. Dudhia, 2006: A new vertical diffusion package with an explicit treatment of entrainment processes. *Mon. Wea. Rev.*, **134**, 2318–2341, https://doi.org/10.1175/MWR3199.1.

Houser, J. L., and H. B. Bluestein, 2011: Polarimetric Doppler radar observations of Kelvin–Helmholtz waves in a winter storm. *J. Atmos. Sci.*, **68**, 1676–1702, https://doi.org/10.1175/2011JAS3566.1.

Houze, R. A. Jr., and S. Medina, 2005: Turbulence as a mechanism for orographic precipitation enhancement. *J. Atmos. Sci.*, **62**, 3599–3623, https://doi.org/10.1175/JAS3555.1.

——, and Coauthors, 2017: The Olympic Mountains Experiment (OLYMPEX). *Bull. Amer. Meteor. Soc.*, **98**, 2167–2188, https://doi.org/10.1175/BAMS-D-16-0182.1.

Iacono, M. J., J. S. Delamere, E. J. Mlawer, M. W. Shephard, S. A. Clough, and W. D. Collins, 2008: Radiative forcing by long-lived greenhouse gases: Calculations with the AER radiative transfer models. *J. Geophys. Res.*, **113**, D13103, https://doi.org/10.1029/2008JD009944.

Kudo, A., 2013: The generation of turbulence below midlevel cloud bases: The effect of cooling due to sublimation of snow.

*J. Appl. Meteor. Climatol.*, **52**, 819–833, https://doi.org/10.1175/JAMC-D-12-0232.1.

Lalas, D. P., and F. Einaudi, 1974: On the correct use of the wet adiabatic lapse rate in the stability criteria of a saturated atmosphere. *J. Appl. Meteor.*, **13**, 318–324, https://doi.org/10.1175/1520-0450(1974)013<0318:OTCUOT>2.0.CO;2.

Mahalov, A., M. Moustaoui, and V. Grubišić, 2011: A numerical study of mountain waves in the upper troposphere and lower stratosphere. *Atmos. Chem. Phys.*, **11**, 5123–5139, https://doi.org/10.5194/acp-11-5123-2011.

Medina, S., and R. A. Houze Jr., 2015: Small-scale precipitation elements in midlatitude cyclones crossing the California Sierra Nevada. *Mon. Wea. Rev.*, **143**, 2842–2870, https://doi.org/10.1175/MWR-D-14-00124.1.

——, and ——, 2016: Kelvin–Helmholtz waves in extratropical cyclones passing over mountain ranges. *Quart. J. Roy. Meteor. Soc.*, **142**, 1311–1319, https://doi.org/10.1002/qj.2734.

Mesinger, F., and Coauthors, 2006: North American Regional Reanalysis. *Bull. Amer. Meteor. Soc.*, **87**, 343–360, https://doi.org/10.1175/BAMS-87-3-343.

Miles, J. W., and L. N. Howard, 1964: Note on a heterogeneous shear flow. *J. Fluid Mech.*, **20**, 331–336, https://doi.org/10.1017/S0022112064001252.

Morrison, H., and J. Milbrandt, 2011: Comparison of two-moment bulk microphysics schemes in idealized supercell thunderstorm simulations. *Mon. Wea. Rev.*, **139**, 1103–1130, https://doi.org/10.1175/2010MWR3433.1.

Na, J. S., E. K. Jin, and J. S. Lee, 2014: Investigation of Kelvin–Helmholtz instability in the stable boundary layer using large eddy simulation. *J. Geophys. Res. Atmos.*, **119**, 7876–7888, https://doi.org/10.1002/2013JD021414.

Nakanishi, M., and H. Niino, 2012: Large-eddy simulation of roll vortices in a hurricane boundary layer. *J. Atmos. Sci.*, **69**, 3558–3575, https://doi.org/10.1175/JAS-D-11-0237.1.

——, R. Shibuya, J. Ito, and H. Niino, 2014: Large-eddy simulation of a residual layer: Low-level jet, convective rolls, and Kelvin–Helmholtz instability. *J. Atmos. Sci.*, **71**, 4473–4491, https://doi.org/10.1175/JAS-D-13-0402.1.

Niu, G.-Y., and Coauthors, 2011: The community Noah land surface model with multiparameterization options (Noah-MP): 1. Model description and evaluation with local-scale measurements. *J. Geophys. Res.*, **116**, D12109, https://doi.org/10.1029/2010JD015139.

Petre, J. M., and J. Verlinde, 2004: Cloud radar observations of Kelvin–Helmholtz instability in a Florida anvil. *Mon. Wea. Rev.*, **132**, 2520–2523, https://doi.org/10.1175/1520-0493(2004)132<2520:CROOKI>2.0.CO;2.

Samelson, R. M., and E. D. Skyllingstad, 2016: Frontogenesis and turbulence: A numerical simulation. *J. Atmos. Sci.*, **73**, 5025–5040, https://doi.org/10.1175/JAS-D-16-0145.1.

Sauer, J. A., D. Muñoz-Esparza, J. Canfield, K. Costigan, R. R. Linn, and Y.-J. Kim, 2016: A large-eddy simulation study of atmospheric boundary layer influence on stratified flows over terrain. *J. Atmos. Sci.*, **73**, 2615–2632, https://doi.org/10.1175/JAS-D-15-0282.1.

Sha, W., T. Kawamura, and H. Ueda, 1991: A numerical study on sea/land breezes as a gravity current: Kelvin–Helmholtz billows and inland penetration of the sea-breeze front. *J. Atmos. Sci.*, **48**, 1649–1665, https://doi.org/10.1175/1520-0469(1991)048<1649:ANSOSB>2.0.CO;2.

Skamarock, W. C., 2004: Evaluating mesoscale NWP models using kinetic energy spectra. *Mon. Wea. Rev.*, **132**, 3019–3032, https://doi.org/10.1175/MWR2830.1.

——, J. B. Klemp, J. Dudhia, D. O. Gill, D. M. Barker, W. Wang, and J. G. Powers, 2005: A description of the Advanced Research WRF version 2. NCAR Tech. Note NCAR/TN-468+STR, 88 pp., https://doi.org/10.5065/D6DZ069T.

——, and Coauthors, 2008: A Description of the Advanced Research WRF version 3. NCAR Tech. Note NCAR/TN-475+STR, 113 pp., https://doi.org/10.5065/D68S4MVH.

——, S. Park, J. B. Klemp, and C. Snyder, 2014: Atmospheric kinetic energy spectra from global high-resolution nonhydrostatic simulations. *J. Atmos. Sci.*, **71**, 4369–4381, https://doi.org/10.1175/JAS-D-14-0114.1.

Smyth, W. D., 2004: Kelvin–Helmholtz billow evolution from a localized source. *Quart. J. Roy. Meteor. Soc.*, **130**, 2753–2766, https://doi.org/10.1256/qj.03.226.

Sykes, R. I., and W. S. Lewellen, 1982: A numerical study of breaking Kelvin-Helmholtz billows using a Reynolds-stress turbulence closure. *J. Atmos. Sci.*, **39**, 1506–1520, https://doi.org/10.1175/1520-0469(1982)039<1506:ANSOBK>2.0.CO;2.

Thompson, G., P. R. Field, R. M. Rasmussen, and W. D. Hall, 2008: Explicit forecasts of winter precipitation using an improved bulk microphysics scheme. Part II: Implementation of a new snow parameterization. *Mon. Wea. Rev.*, **136**, 5095–5115, https://doi.org/10.1175/2008MWR2387.1.

Thompson, W. T., T. Holt, and J. Pullen, 2007: Investigation of a sea breeze front in an urban environment. *Quart. J. Roy. Meteor. Soc.*, **133**, 579–594, https://doi.org/10.1002/qj.52.

Trier, S. B., R. Sharman, and T. P. Lane, 2012: Influences of moist convection on a cold-season outbreak of clear-air turbulence (CAT). *Mon. Wea. Rev.*, **140**, 2477–2496, https://doi.org/10.1175/MWR-D-11-00353.1.

Wakimoto, R. M., W. Blier, and C. Liu, 1992: The frontal structures of an explosive oceanic cyclone: Airborne radar observation of ERICA IOP 4. *Mon. Wea. Rev.*, **120**, 1135–1155, https://doi.org/10.1175/1520-0493(1992)120<1135:TFSOAE>2.0.CO;2.

Weckwerth, T. M., and R. M. Wakimoto, 1992: The initiation and organization of convective cells atop a cold-air outflow boundary. *Mon. Wea. Rev.*, **120**, 2169–2187, https://doi.org/10.1175/1520-0493(1992)120<2169:TIAOOC>2.0.CO;2.

Zhou, B., and F. K. Chow, 2013: Nighttime turbulent events in a steep valley: A nested large-eddy simulation study. *J. Atmos. Sci.*, **70**, 3262–3276, https://doi.org/10.1175/JAS-D-13-02.1.